Mass-conserved volumetric lattice Boltzmann method for complex flows with willfully moving boundaries

Huidan Yu,[1,*] Xi Chen,[1] Zhiqiang Wang,[2] Debanjan Deep,[1] Everton Lima,[3] Ye Zhao,[2] and Shawn D. Teague[4]
[1]*Department of Mechanical Engineering, Indiana University-Purdue University Indianapolis, Indianapolis, Indiana 46202, USA*
[2]*Department of Computer Science, Kent State University, Kent, Ohio 44240, USA*
[3]*Department of Computer and Information Science, Indiana University-Purdue University Indianapolis, Indianapolis, Indiana 46202, USA*
[4]*Department of Radiology and Imaging Sciences, Indiana University School of Medicine, Indianapolis, Indiana 46202, USA*
(Received 9 October 2012; revised manuscript received 21 April 2014; published 11 June 2014)

In this paper, we develop a mass-conserved volumetric lattice Boltzmann method (MCVLBM) for numerically solving fluid dynamics with willfully moving arbitrary boundaries. In MCVLBM, fluid particles are uniformly distributed in lattice cells and the lattice Boltzmann equations deal with the time evolution of the particle distribution function. By introducing a volumetric parameter $\mathcal{P}(x,y,z,t)$ defined as the occupation of solid volume in the cell, we distinguish three types of lattice cells in the simulation domain: solid cell (pure solid occupation, $\mathcal{P}=1$), fluid cell (pure fluid occupation, $\mathcal{P}=0$), and boundary cell (partial solid and partial fluid, $0<\mathcal{P}<1$). The formulation of volumetric lattice Boltzmann equations are self-regularized through $\mathcal{P}$ and consist of three parts: (1) collision taking into account the momentum exchange between the willfully moving boundary and the flow; (2) streaming accompanying a volumetric bounce-back procedure in boundary cells; and (3) boundary-induced volumetric fluid migration moving the residual fluid particles into the flow domain when the boundary swipes over a boundary cell toward a solid cell. The MCVLBM strictly satisfies mass conservation and can handle irregular boundary orientation and motion with respect to the mesh. Validation studies are carried out in four cases. The first is to simulate fluid dynamics in syringes focusing on how MCVLBM captures the underlying physics of flow driven by a willfully moving piston. The second and third cases are two-dimensional (2D) peristaltic flow and three-dimensional (3D) pipe flow, respectively. In each case, we compare the MCVLBM simulation result with the analytical solution and achieve quantitatively good agreements. The fourth case is to simulate blood flow in human aortic arteries with a very complicated irregular boundary. We study steady flow in two dimensions and unsteady flow via the pulsation of the cardiac cycle in three dimensions. In the 2D case, both vector (velocity) and scalar (pressure) fields are compared to computation results from a well-established Navier-Stokes solver and reasonably good agreements are obtained. In the 3D case, the unsteady flow pattern and wall shear stress are well captured at the representative time instants during the pulsation. The validations demonstrate that the MCVLBM is a relatively simple but reliable computation scheme to deal with static or moving irregular boundaries.

DOI: 10.1103/PhysRevE.89.063304 PACS number(s): 47.11.−j, 47.27.ek, 47.63.Cb

I. INTRODUCTION

The recent development of the lattice Boltzmann method (LBM) [1–3] has prompted tremendous advancements in its capabilities to systematically model and simulate complex flow properties [4–6]. The well-recognized advantages of LBM include the capability to model multiphase flow, the ease in treating complex boundaries, and the suitability to implement massive parallel computing. The interaction of a fluid with a rigid or elastic structure [7] is of crucial significance in engineering, ecological, and biomechanics systems. Damages associated with flow-induced vibrations [8] in aircraft wings, bridges, or tall buildings can be catastrophic. Understanding the mechanisms of fluid-structure interaction (FSI) between wind and the elastic vibrations of blades is critical for enhancing the efficiency of wind energy generation [9]. Mechanical interactions between wind and plant organs or systems [10] have been a major concern for humankind over the ages due to the impact on the human living environment. In biomechanics, correlations between an internal flow and wall deformation often underlie a vessel's biological function or dysfunction [11–14] due to the fact that almost all vessels carrying fluids within the body are flexible. In most practical cases, the interface between fluid and structure is irregular and moving willfully and/or compliantly.

The LBM solves flow dynamics through prescribed discrete kinetic equations for time evolution of discrete particle density distribution functions due to molecular interaction, i.e., the lattice Boltzmann equation (LBE). The macroscopic flow properties are the direct results of the moments of these particle density distribution functions. Mathematically the LBE is a specially discretized representation of the Boltzmann equation and it recovers Navier-Stokes (NS) equations up to the second order of accuracy in space and time in the incompressible limit [15,16]. Recently, it has been demonstrated that through a moment expansion procedure, the LBM can be extended to solve compressible fluid dynamics and complex flow beyond NS equations [17]. At a fluid-structure interface, the enforcement of boundary conditions in LBM is conceptually straightforward [18,19]: a simple bounce-back after fluid particles hit the structure reverses all particle momentums such that the nonslip boundary condition is realized; whereas a particle specular reflection process that reverses the normal momentum component and maintains the tangential counterpart reflects the free-slip boundary condition [20].

The conventional LBM is node based. Fluid particles are sitting at lattice nodes. The particle distribution functions

*whyu@iupui.edu

represent the particle density distributions associated with discrete molecular velocities. In the time evolution, particles collide at the nodes and then stream from the current node to the prescribed finite neighboring nodes along their velocity directions. The well-established LBE with a Bhatnagar-Gross-Krook (BGK) collision operator is written as the following [2,3]:

$$f_i(\vec{x}+\vec{e}_i\triangle t, t+\triangle t) = f_i(\vec{x},t) + \Omega_i(\vec{x},t) \tag{1}$$

$$\Omega_i(\vec{x},t) = -\frac{f_i(\vec{x},t) - f_i^{\mathrm{eq}}(\vec{x},t)}{\tau}, \tag{2}$$

where $\vec{e}_i$ is the prescribed discrete molecular velocity in the ith direction ($i = 0,1,\ldots,b$) and τ is the single relaxation time. The time-evolving procedure includes two sequential processes: (1) a collision during which particles at the located node interact with each other so as to increase the local entropy while conserving mass, momentum, and energy conservation, and (2) a streaming during which the particle moves to the prescribed neighboring nodes according to their molecular velocity directions. It has been shown that LBM is second-order accurate in both space and time [5].

The bounce-back boundary condition and its extensions to curved boundaries, thermal boundaries, and so on on the node-based description have generally been found to work well [20–31] for fixed rigid boundaries. Ladd was the first to develop a moving boundary scheme [32], specifically for suspension flows. The method introduces an additional term along the bounce-back direction to account for the momentum exchange between the fluid and moving solid boundary. Later, Bouzidi *et al.* [33] proposed an LBE boundary condition for moving boundaries by combination of the bounce-back scheme and spatial interpolations of first or second order. Recently, Yin and Zhang [34] further improved the bounce-back scheme with velocity interpolation/extrapolation for moving boundaries with more complicated geometries. Instead of interpolating boundary density distribution functions as in Bouzidi's boundary condition [33], they evaluated the velocity at the midpoint of the boundary lattice link via interpolation or extrapolation, depending on the orientation of the local boundary, from the desired boundary velocity at the boundary node and the fluid velocity at a fluid node near the boundary. The bases of these schemes to deal with the curved boundary that cuts the lattice off nodes are either point-wise particle density distribution interpolation or particle density distribution transformation into local curve-linear coordinate systems. As a result, most of these schemes do not have exact conservations of mass and momentum and might fail to maintain the detailed balance among particle density distributions. For arbitrary curved structures, the resulting numerical artifacts may contaminate the physics of fluid dynamics [25–27]. Moreover, the realization of high-order interpolations involving nonlocal information is difficult and inefficient in general complex flows. Aidun *et al.* [35] have tried to modify Ladd's method to formulate an impermeable boundary treatment with no mass exchange across the boundary, while taking into account the momentum exchange between the fluid and the solid particle. However, like the Ladd approach, mass is only strictly conserved when solid boundaries cover and uncover equal fluid volumes simultaneously. The diffusive bounce-back condition [36,37] is another viewpoint to realize no-slip boundary condition on the lattice Boltzmann platform based on kinetic theory. Instead of imposing the no-slip condition, the diffusive bounce-back condition [36] specifies a boundary condition which ensures positive-definite populations with the same concept of diffusive boundary condition while retaining the simplicity of bounce-back technique. A recently developed hybrid diffusive-bounce-back boundary condition [37] achieved considerable enhancement in the accuracy of the unsteady force calculation at moderate and high Reynolds numbers. Regardless of the successful applications of node-based LBM for suspension flows where the moving structures are generally rigid and regular such as spheres. When the structure is arbitrary in three dimensions, the required interpolation or extrapolation in node-based LBM becomes rather challenging.

The volumetric concept of LBM was specifically introduced for arbitrary moving boundaries [18]. In fact, the continuous bounce-back method Verberg and Ladd developed [38,39] is a type of volumetric representation. In volumetric lattice Boltzmann representation, fluid particles are uniformly distributed in each lattice cell, instead of sitting at the grid nodes in conventional LBM. The interface, i.e., the boundary of the fluid, where the structure cuts the flow field is determined by the occupation of solid percentage volume in each cell. The solid percentage in a cell can achieve better control of various hydrodynamic flux in or out of the cell and guarantee the exact conservation of mass and momentum in the fluid domain. The numerical artifacts in boundary discretization and interpolation as employed in node-based LBM can be greatly suppressed [19,40]. There have been efforts to extend volumetric representation in LBM for arbitrary curved boundaries. An efficient fractional volumetric scheme [41] combining the mass-conserved volumetric lattice Boltzmann method (MCVLBM) [19] with a fractional propagation scheme [42] was proposed to improve the stability of the thermal LBM while keeping the accuracy and simplicity of the original LBM. A volumetric boundary condition [18] was extended [43] by introducing a local velocity-gradient-based correction to the original evenly bounced-back particles and successfully simulated flow past an impulsively started circular cylinder at low and moderate Reynolds numbers. Recently, the boundary condition was further developed to a generalized volumetric boundary algorithm [44] and validated by vortex shedding simulation from a circular cylinder by the same group.

In this paper, we develop an MCVLBM for willfully moving arbitrary boundaries in FSI systems. Here "willfully moving" means the boundary moves with prior defined velocity, whereas "compliantly moving" means the boundary is driven to move by the fluid. The MCVLBM consists of three operations. First, the generalized collision in which the momentum exchange between the fluid and moving boundary (structure) are accounted for. Second, generalized streaming including a volumetric bounce-back treatment where fluid and the structure interact. Third, which is new to conventional node-based LBM, boundary-induced migration to distribute the residual fluid into the adjacent fluid region as the boundary swipes the fluid domain. The third operation is introduced to ensures mass conservation in the fluid domain when the

boundary moves. This approach can handle arbitrary boundary orientation and motion with respect to the mesh. To distinguish fluid, solid, and boundary lattice cells, we introduce a parameter $\mathcal{P}(\vec{x},t)$ to determine the composition ratio of solid versus liquid in each cell. The volumetric lattice Boltzmann equations are formulated based on $\mathcal{P}(\vec{x},t)$ for all three operations, thus the implementation of the MCVLBM is significantly simpler comparing the existing LBM schemes for moving arbitrary boundaries. To validate the proposed MCVLBM, we carry out four application studies: fluid dynamics in syringes where fluid is driven by a moving piston, two-dimensional (2D) peristaltic flow driven by wall propagation, three-dimensional (3D) pipe flow, and 2D and 3D blood flow in patient-specific normal aorta. Quantitative comparisons between MCVLBM and analytical solutions and qualitative comparisons between MCVLBM and an established NS solver are made, respectively. Satisfactory agreements are achieved.

The remainder of the paper is organized as follows. Section II develops the mathematical formulation of MCVLBM including three processes: collision, streaming, and migration. Four validation studies and quantitative and qualitative comparisons are presented in Sec. III. Finally Sec. IV provides a summary discussion and concludes the paper.

II. MATHEMATICAL FORMULATION OF MASS-CONSERVED VOLUMETRIC LATTICE BOLTZMANN METHOD

In general, the LBM consists of a finite discrete set of particle velocities $\vec{e}_i$ $(i = 0,\ldots,b)$, defined on a D-dimensional lattice Γ, as illustrated in Fig. 1 for the D2Q9 lattice model. Such a lattice consists of equally shaped cells and each cell occupies a spatial domain $D(\vec{x})$ with volume $\triangle v = (\triangle l^D)$. In conventional LBM, particles are sitting at lattice nodes $\vec{x}$, see Fig. 1(a). The function $f_i(\vec{x},t)$ represents the particle density distribution associated with the velocity $\vec{e}_i$. During each elementary time step $\triangle t$, particles at node $\vec{x}$ collide and then stream to the neighboring nodes $\vec{x} + \vec{e}_i\triangle t (i = 1,\ldots,b)$ along their velocity directions.

Alternatively, we employ the volumetric representation in which particles are considered to be uniformly distributed in lattice cells as shown in Fig. 1(b). If a flow involves moving boundaries, the fluid domain will be continuously changing as the boundaries move across the fluid domain. Fluid particles distributed within cells where the boundary is located will be

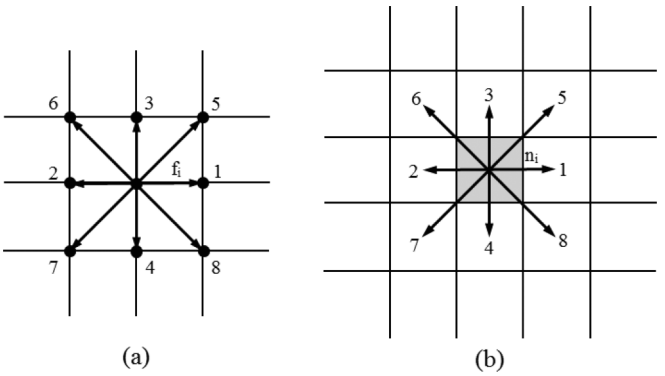

FIG. 1. Illustration of (a) node-based lattice and (b) volume-based lattice on D2Q9 lattice model.

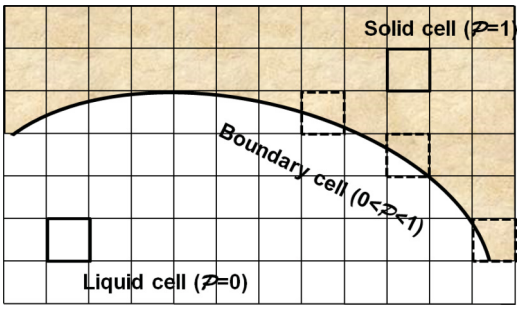

FIG. 2. (Color online) Illustration of solid ($\mathcal{P} = 1$), fluid ($\mathcal{P} = 0$), and boundary ($0 < \mathcal{P} < 1$) cells in a volumetric domain where $\mathcal{P}$ is the portion of the solid in a lattice cell.

thus covering or uncovering. In MCVLBM, we introduce the function $n_i(\vec{x},t)$ representing the particle distribution function with velocity $\vec{e}_i$ occupying a lattice cell $\vec{x}$ at time t and deal with the time evolution of the particle distribution function analogy to LBE, i.e., Eq. (1)

$$n_i(\vec{x} + \vec{e}_i\Delta\, t, t + \Delta t) = n_i(\vec{x},t) + \Omega_i(\vec{x},t), \tag{3}$$

where $\Omega_i(\vec{x},t)$ is a collision term related to the change of the particle distribution function due to molecular motion and the momentum exchange between flow and the moving boundary. For a fluid cell, particle distribution function n_i and particle density distribution function f_i have the same value if the volume of the cell $\triangle V$ is taken to be unity.

Cells adjacent to the moving boundary may be occupied entirely by either a solid or fluid, while others may have partial fluid and partial solid volumes. In the entire domain, cells can be categorized through the occupation of solid volume in the cell, defined by $\mathcal{P}(\vec{x},t) \equiv \triangle V_s(\vec{x},t)/\triangle V$. Figure 2 illustrates three distinct cell types adjacent to a boundary: fluid cell ($\mathcal{P} = 0$, fluid only), solid cell ($\mathcal{P} = 1$, solid only), and boundary cell ($0 < \mathcal{P} < 1$, partially solid and partially fluid,). When the boundary moves, cell type may change in time along with the volume fractions of the solid in the cell. Some cells are being covered by the moving boundary while some other cells are being uncovered. A boundary cell may become a solid cell or fluid cell depending on the moving direction of the boundary. The fluid volume portion of the cell is therefore

$$\triangle V_f(\vec{x},t) = [1 - \mathcal{P}(\vec{x},t)]\triangle V. \tag{4}$$

It is noted that the relation between the particle density distribution function f_i in traditional node-based LBM and the particle distribution function n_i in the volumetric LBM is as follows:

$$f_i(\vec{x},t) = n_i(\vec{x},t)/\triangle V_f(\vec{x},t). \tag{5}$$

With the described volumetric representation we construct the mass-conserved volumetric lattice Boltzmann equation, i.e., Eq. (3), through the following three processes, which uniquely takes into account the moving arbitrary boundary.

A. Collision including willfully moving boundary

We first write the right-hand side of Eq. (3) as

$$n_i'(\vec{x},t) = n_i(\vec{x},t) + \Omega_i(\vec{x},t), \tag{6}$$

where $n_i'(\vec{x},t)$ represents the "postcollision" particle distribution function. The most convenient choice for $\Omega_i(\vec{x},t)$ is the BGK model with a single time scale of relaxation

$$\Omega_i(\vec{x},t) = -\frac{1}{\tau}[n_i(\vec{x},t) - n_i^{\rm eq}(\vec{x},t)], \tag{7}$$

where the equilibrium particle distribution function $n_i^{\rm eq}(\vec{x},\, t)$ is formulated as

$$n_i^{\rm eq}(\vec{x},t) = N\omega_i\left[1 + \frac{\vec{e}_i\cdot\vec{U}}{c_s^2} + \frac{(\vec{e}_i\cdot\vec{U})^2}{2c_s^4} - \frac{\vec{U}\cdot\vec{U}}{2c_s^2}\right], \tag{8}$$

where ω_i is an appropriate weight of the ith velocity direction, c_s is the sound speed, and $N(\vec{x},t) = \sum n_i(\vec{x},t)$.

To take into account the momentum change from a moving boundary, we replace the macroscopic fluid velocity $\vec{u}$ by $\vec{U} = \vec{u} + \delta\vec{u}$ (according to the macroscopic physical collision it processes empirically) in the formulation of equilibrium particle distribution function, where

$$\delta\vec{u} = \tau\mathcal{P}(\vec{x},t)\vec{u}_b(\vec{x},t) + \frac{\tau\sum_{j=1}^{b}\mathcal{P}(\vec{x}+\vec{e}_j,t)n_j(\vec{x},t)\vec{u}_b(\vec{x}+\vec{e}_j,t)}{N(\vec{x},t)}, \tag{9}$$

with $\vec{u}_b(\vec{x},t)$ being the average velocity of the boundary in cell $\vec{x}$ at time t. This equation was constructed on an empirical basis. The first part of the right-hand side is the change of fluid velocity due to the moving of the solid portion in the current cell and the second part is the bounced-back particles which are streaming to the neighboring cells. The bounce-back particles carry the amount of momentum changes due to the moving boundaries that are proportional to the interaction time and relative fraction of the bounced-back particles. Equation (9) accounts for the momentum transfer induced by boundary movement, but no extra mass is introduced. From Eqs. (6) to (9), one can obtain the momentum in a cell $\vec{x}$ after collision $N\vec{u} + \mathcal{P}N\vec{u}_b + \sum_{j=1}^{b}\mathcal{P}(\vec{x}+\vec{e}_j,t)n_j(\vec{x},t)\vec{u}_b(\vec{x}+\vec{e}_j,t)$. The terms related to $\vec{u}_b$ identify the momentum transfer between the fluid and solid when the latter is moving. It is noted that either interior fluid cells ($\mathcal{P}=0$) or stationary boundary ($\vec{u}_b \equiv 0$) results in $\delta\vec{u} = 0$ in Eq. (9). In these two cases, Eq. (6) is identical to the node-based LBE for collision operation.

B. Streaming including bounce-back boundary condition

Streaming means particles moving from the current cell to neighboring cells. Since a boundary cell is generally occupied partially by fluid, only an appropriate volume fraction of fluid particles will be able to stream to its neighboring cell, determined by the fluid fraction of the receiving cell. The volume fraction streaming is illustrated in Fig. 3. Considering n_i particles stream from cell A to cell B in the ith direction, assume the solid fraction of cell B is $\mathcal{P}_B$, the receiving of these particles depends on the fluid fraction of cell B, i.e., $(1-\mathcal{P}_B)n_i$, and $\mathcal{P}_B n_i$ particles will be bounced back to cell A in the opposite direction. If cell B is a fluid cell with $\mathcal{P}_B = 0$, all n_i will stream in and there will be no bounce-back, thus the streaming process is identical to the node-based LBE for the streaming operation. As a result, particles in cell $\vec{x}$ at time $t+\triangle t$ after the streaming operation are from two sources: (i) streaming from its upwind neighboring cells

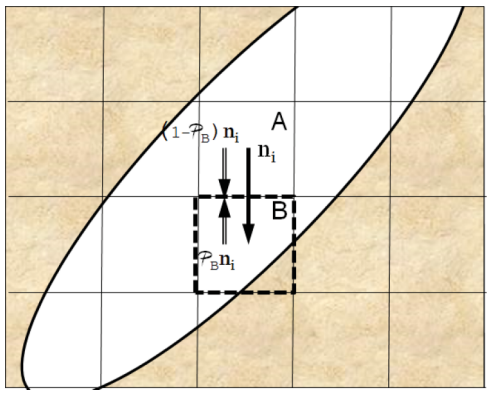

FIG. 3. (Color online) Illustration of volume fraction streaming: considering n_i particles stream from cell A to cell B in the ith direction. Assuming the solid fraction of cell B is $\mathcal{P}_B$, the receiving of these particles depends on the fluid fraction of cell B, i.e., $(1-\mathcal{P}_B)n_i$, and $\mathcal{P}_B n_i$ particles will be bounced back to cell A in the opposite direction.

$[1-\mathcal{P}(\vec{x},t)]n_i'(\vec{x}-\vec{e}_i\Delta t,t)$, and (ii) bounce-back from the downwind cells $\mathcal{P}(\vec{x}+\vec{e}_{i*}\Delta t,t)n_{i*}'(\vec{x},t)$, as shown in Eq. (10) below

$$n_i''(\vec{x},t+\triangle t) = [1-\mathcal{P}(\vec{x},t)]n_i'(\vec{x}-\vec{e}_i\Delta t,t) + \mathcal{P}(\vec{x}+\vec{e}_{i*}\Delta t,t)n_{i*}'(\vec{x},t), \tag{10}$$

where i^* corresponds to the particle velocity direction opposite to the ith direction. That is $\vec{e}_{i^*} = -\vec{e}_i$. This modified streaming process ensures that particles are advected or reflected to their appropriate places in the fluid domain but does not introduce any extra mass. When $\mathcal{P}(\vec{x},t) = 0$, the above equation reduces to node-based LB form where only upwind streaming occurs.

C. Boundary-induced migration of particles

The generalized streaming process including the bounce-back of particles described above is not sufficient to ensure mass conservation in the fluid domain. As a boundary crosses a boundary cell, the fraction of solid volume in the cell increases until it eventually becomes a solid cell, e.g., the dashed cells in Fig. 4. At the instant that the boundary cell becomes a solid cell, there might be fluid particles left behind. For instance,

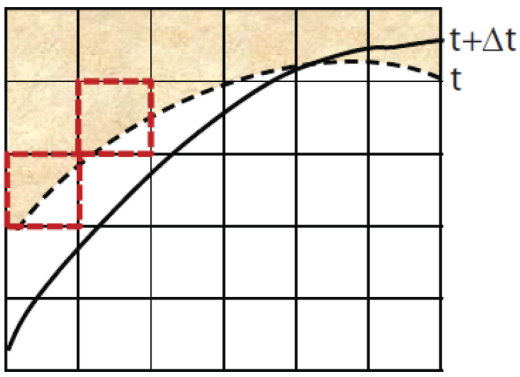

FIG. 4. (Color online) Boundary cells (dashed) at time t become solid cells at $t+\triangle t$ due to the moving of the boundary.

the rest particles that are not part of the streaming process will be stayed, and a few nonrest particles which may remain from the streaming process as the boundary moves through the cell according to Eq. (10); these fluid particles must be migrated into the fluid domain. The migration may be formulated as follows:

$$n_i(\vec{x},t+\Delta t) = [1-\mathcal{P}'(\vec{x},t+\Delta t)]n_i''(\vec{x},t+\Delta t) + \sum_{j=1}^{b} n_{i,j}^{*}(\vec{x}-\vec{e}_i\Delta t,t+\Delta t), \quad (11)$$

where $i = 0,1,\ldots,b$ and

$$n_{i,j}^{*}(\vec{x},t+\Delta t) = \mathcal{P}'(\vec{x},t+\Delta t)n_i''(\vec{x},t+\Delta t) \times [1-\mathcal{P}'(\vec{x}+\vec{e}_j\Delta t,t)]n_j'(\vec{x},t)/ \times \sum_{k=1}^{b}[1-\mathcal{P}'(\vec{x}+\vec{e}_k\Delta t,t)]n_k'(\vec{x},t). \quad (12)$$

In the above, $\mathcal{P}'$ is the fraction of particles in cell $\vec{x}$. When the boundary is covering a boundary cell, we force $\mathcal{P}'$ part ($\mathcal{P}'=0$ for the fluid cell, $\mathcal{P}'=1$ for the solid cell, and $0<\mathcal{P}'<1$ for the surface cell) of the total particles in cell $\vec{x}$, the second term at the right -hand side of Eq. (11) after streaming migrates to its neighboring cells according to the particle distribution specified by Eq. (12). Although the variation of $\mathcal{P}'$ from time step to time step is not unique, it must be modeled in such a way as to guarantee that no particles remain in the cell when it becomes a purely solid cell, i.e., finally the surface cell becomes a purely solid cell, namely, $\mathcal{P}(\vec{x},t)=1$. Equation (11) insures all particles remaining in cell $\vec{x}$ migrating out, which make mass conserve in the flow field.

In our analysis we model $\mathcal{P}'$ as

$$\mathcal{P}' = \mathcal{P}\alpha/[\mathcal{P}+a(1-\mathcal{P})], \quad (13)$$

with $\alpha=1$ for $\mathcal{P}(\vec{x},t)-\mathcal{P}(\vec{x},t-\Delta t)>0$, and $\alpha=0$ for $\mathcal{P}(\vec{x},t)-\mathcal{P}(\vec{x},t-\Delta t)\leqslant 0$ so that the boundary-induced particle migration only operates when solid fractions in boundary cells are increasing in time. The parameter a is introduced to adjust the rate of the particle migration when the boundary cuts into the flow domain corresponding to $\alpha=1$ in Eq. (13). It is noted that Eq. (13) is an empirical model. Instead of migrating the residual particles out at the last time step when a boundary cell becomes a solid cell, the introduction of $\mathcal{P}'$ allows particle migration at time steps when the fluid domain is covered. As shown in Fig. 5, when a increases, more fluid particles are migrated when $\mathcal{P}$ closes to 1, whereas small a results in early migration before the boundary cells become a solid cell. This model is effective to reduce pressure fluctuation when the row or column in the fluid domain is uniform, as discussed below.

The resulting density, velocity, and pressure are obtained as follows:

$$\rho(\vec{x},t) = \sum n_i(\vec{x},t)/[1-\mathcal{P}(\vec{x},t)], \quad (14)$$

$$\vec{u}(\vec{x},t) = \sum e_i n_i(\vec{x},t)/\sum n_i(\vec{x},t), \quad (15)$$

and

$$p(\vec{x},t)-p_0 = c_s^2[\rho(\vec{x},t)-\rho_0], \quad (16)$$

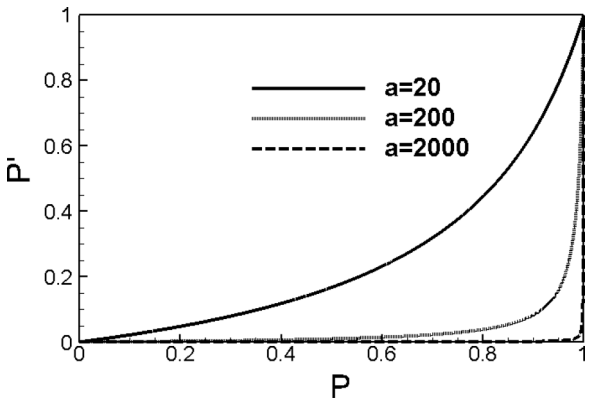

FIG. 5. Parameterizations of $\mathcal{P}'$ by $\mathcal{P}$ for different a's. $\mathcal{P}'=\mathcal{P}/[\mathcal{P}+a(1-\mathcal{P})]$.

where p_0 and $\rho_0(=1)$ are reference pressure and density respectively.

III. APPLICATION STUDIES FOR VALIDATION

We perform four application studies to validate MCVLBM: flow in a syringe and peristaltic flow for a moving boundary (2D), pipe flow for a curved boundary (3D), and blood flow in a human aorta for an arbitrary boundary in 2D and 3D, respectively. For the 2D cases, we use the two-dimensional nine-velocity (D2Q9) lattice model [2] with $b=8$, see Fig. 1(b). The discrete particle velocities $\vec{e}_i$ and the weighting factor ω_i ($i=0,1,2,\ldots,8$) are $\vec{e}_i=(0,0)\sqrt{3}c_s$ and $\omega_i=4/9$ for $i=0$, $\vec{e}_i=(\cos[(i-1)\pi/2],\sin[(i-1)\pi/2])\sqrt{3}c_s$, and $\omega_i=1/9$ for $i=1,2,3,4$, and $\vec{e}_i=(\cos[(i-5)\pi/2+\pi/4],\sin[(i-5)\pi/2+\pi/4])\sqrt{3}c_s$ and $\omega_i=1/36$ for $i=5,6,7,8$. Whereas for the 3D case, we use the three-dimensional nineteen-velocity (D3Q19) lattice model with $b=18$ [42]. The discrete particle velocities $\vec{e}_i$ and the weighting factor ω_i ($i=0,1,2,\ldots,18$) are $\vec{e}_i=(0,0)\sqrt{3}c_s$ and $\omega_i=1/3$ for $i=0$, $\vec{e}_i=(\pm1,0,0)\sqrt{3}c_s,(0,\pm1,0)\sqrt{3}c_s,(0,0,\pm1)\sqrt{3}c_s$ and $\omega_i=1/18$ for $i=1-6$, and $\vec{e}_i=(\pm1,\pm1,0)\sqrt{3}c_s,(\pm1,0,\pm1)\sqrt{3}c_s,(0,\pm1,\pm1)\sqrt{3}c_s$, and $\omega_i=1/36$ for $i=7-18$. In both dimensions, $c_s=\frac{1}{\sqrt{3}}$ in Eq. (8). In all cases the Mach numbers are less than 0.03.

A. Fluid dynamics in syringes

The schematic of a syringe geometry together with its nomenclature is illustrated in Fig. 6. The piston serves as a

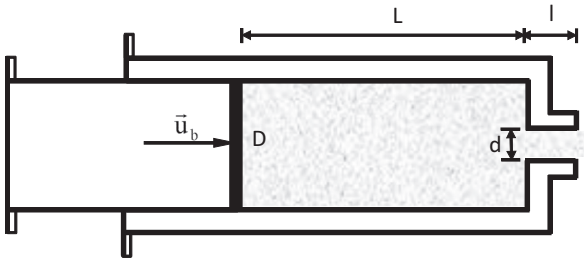

FIG. 6. Schematics of a syringe geometry and nomenclature. The flow is driven by the piston moving with velocity $\vec{u}_b$.

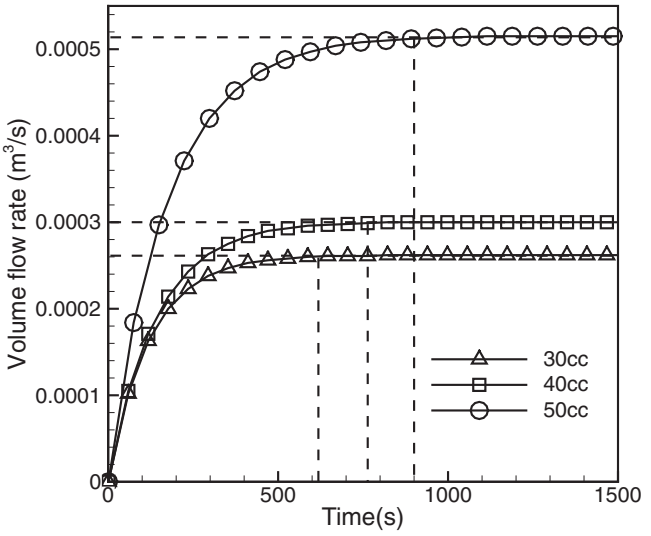

FIG. 7. Time evolution of volume flux in three syringes with sizes of 30, 40, and 50 cc (1 cc = 1 mL = 1000 mm^3).

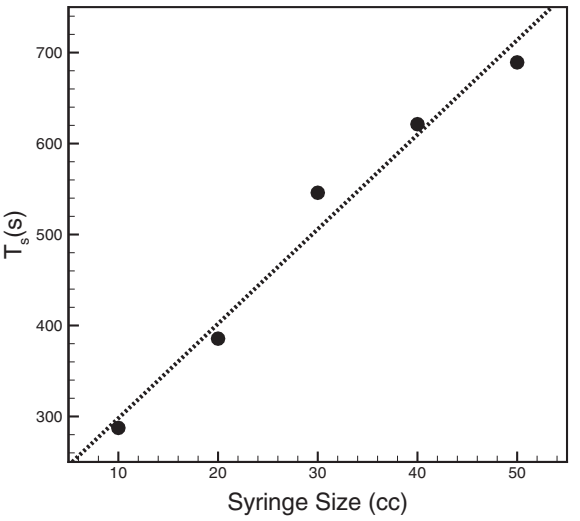

FIG. 8. Linearity between the time to reach steady state and syringe size.

moving boundary with a constant velocity $\vec{u}_b$. The flow is driven by the piston from left to right and discharges at the narrowed exit on the right. When the piston moves, a column of cells is cut simultaneously. In this case, the Reynolds number is relatively small and the flow is laminar. We apply pressure (density) and the velocity flow boundary condition [24] at the outlet where density is specified to be a constant ρ_0 and the exit velocity vectors are forced to be parallel. In addition, there is a no-slip boundary at the top and bottom walls. The boundary condition at the inner piston is automatically taken care of in the collision, Eqs. (8) and (9) for a moving boundary and streaming in Eq. (10) for the no-slip boundary condition.

To check the mass conservation when the piston covers the boundary cells, we first close the exit and evaluate the total fluid mass in the flow domain when the piston moves. It is confirmed that the mass is strictly conserved. The fluid volume ejected at the exit should balance the fluid volume driven forward by the piston at each time step. Figure 7 shows the time evolution of volume flux in three syringes with sizes 30, 40, and 50 cc, 1 cc = 1 mL = 1000 mm^3, respectively. The three sizes are obtained through coherent adjustments of length L and diameter D for target syringe size $V = \pi(D/2)^2 L$. Each horizontal dashed line corresponds to the volume flux driven by the piston to push the fluid forward for the given syringe size. It is seen that in each syringe the volume flux at the piston side and the syringe exit are balanced after the flow becomes steady, which again demonstrates the mass conservation of the fluid. The existence of an unsteady adjustment period in each syringe right after the piston motion is initiated is observed. This initial adjustment period is to be expected and does not violate mass conservation. It is due to the fact that the LBM is a weakly compressible fluid solver where mass density fluctuations in the fluid domain creates compressible sound waves that bring the system to a nearly incompressible equilibrium state. The vertical solid lines indicate the time when the flow reaches a steady state in the syringes, respectively. The time T_s depends on the syringe size, the larger the size of the syringe, the longer T_s. Close examinations show that T_s is linear to the size of the syringe as shown in Fig. 8. Such an adjustment time is somehow real in nursing practice because the same linear relation was observed in experimental measurements [45]. This is due to the fact that any fluid is compressible, more or less.

Figure 9 shows the streamline distribution in a syringe at a time when the aspect ratio of length to diameter is sufficiently large and thus fully developed flow between the piston and syringe exit can be reached. It is seen that the velocity profile in the center of the syringe is close to parabolic, while deviating from parabolic near the piston and at the exit. The transition in the flow pattern in these two regions compares well to the calculation by Watson *et al.* [47] for an axisymmetric syringe flow using a finite difference method. The small eddies observed in the corners are called Moffatt-type eddies [46], which were not detected in the corresponding axisymmetric simulations since the strengths of the eddies were not strong enough, as Watson indicated.

Localized spurious fluctuations in density, and therefore in pressure since $p = c_s^2 \rho$ in LBM, are observed when the moving boundary cross a boundary cell. This periodic discontinuity is due to the migration substep formulated as Eq. (4). Figure 10 shows the time evolution of the relative density difference, defined as $\Delta\rho = |\rho(\vec{x},t) - \rho_0|/\rho_0$, in the boundary cell at the center. The spurious fluctuation appears periodically due to the fact that the piston crosses all the boundary cells aligned in the vertical direction simultaneously.

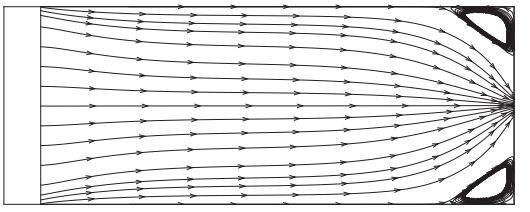

FIG. 9. Streamline distribution in a 25-cc syringe. The corner eddies are called Moffatt-type eddies [46].

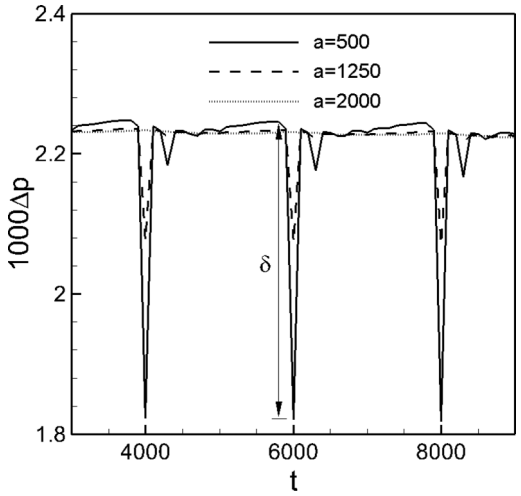

FIG. 10. Time evolution of density (pressure) fluctuation $1000\Delta\rho(=|\rho(t)-\rho_0|/\rho_0)$ in the center boundary cell when $a = 500$ (solid line), $a = 1250$ (dashed line), and $a = 2000$ (dotted line). δ measures the drop of $1000\Delta\rho$ when the moving boundary cuts through a boundary cell.

If we use δ to measure the drop of $1000\Delta\rho$, we find that δ can be dramatically reduced by adjusting the parameter a in Eq. (13). The fluctuation level is large when $a = 500$ (solid line). It drops by more than half when a increases to 1250 (dashed line). When $a = 2000$ (dotted line), the spurious fluctuation is literally removed. In Fig. 11 we show the density fluctuation levels in the boundary cell b, the first and second fluid cells $b+1$ and $b+2$, respectively, as a function of parameter a. It is seen that the spurious density (pressure) fluctuation also affects the flow field adjacent to the moving boundary, but can be suppressed dramatically by increasing parameter a. It should be pointed out that the adjustment of a of Eq. (13) is empirical to adjust the paretical migration rate when the boundary is cutting through a boundary cell. When the flow domain is arbitrary, the paretical migration varies in space and time, thus the spurious density fluctuation is expected to be much less insignificant than the case being discussed.

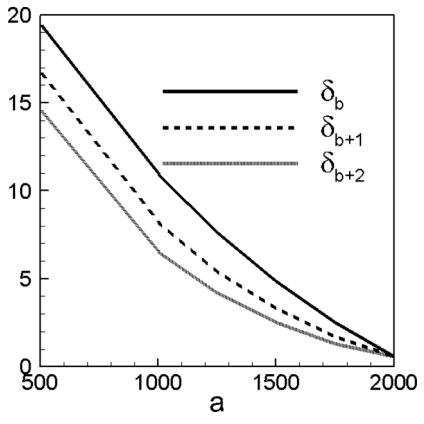

FIG. 11. The dependency of the periodic density (pressure) drop δ on parameter a. Three measured cells are the boundary cell b and two next fluid cells $b+1$ and $b+2$, respectively, on the center line.

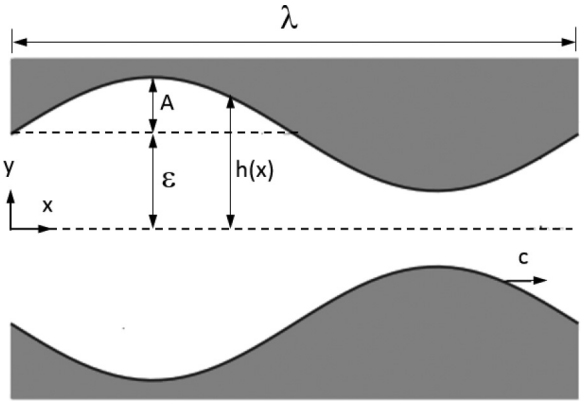

FIG. 12. Geometry and nomenclature for a 2D peristaltic flow.

B. 2D peristaltic flow and 3D pipe flow with analytical solution

In this section, we apply the MCVLBM to 2D peristaltic flow and 3D pipe flow, respectively. Quantitative comparisons with the analytical solutions are made for validation of MCVLBM.

The geometric configuration and nomenclature for a 2D peristaltic flow is shown in Fig. 12. The peristaltic walls are sinusoidal and symmetric to the centerline of the chancel. A transverse wave of deformation alternately contracts and expands the wall position as it progresses with a constant speed c in the horizontal direction. The shape of the peristaltic wall is measured as

$$h(x,t) = \varepsilon + A\cos[2\pi(x-ct)/\lambda], \tag{17}$$

where λ, ε, and A are the wavelength, the half width of the channel, and the amplitude of the wall deformation. The wall motion is constrained to be in the vertical direction whereas the wave propagates horizontally. The dimensionless time-mean volume flow at a cross section located at x can be obtained via an integral over one full period of peristalsis

$$\Phi(x) = \frac{1}{\varepsilon cT}\int_0^T\int_0^h u(y,t)dydt, \tag{18}$$

where $T = \lambda/c$ is the period. Shapiro *et al.* [48] and Jaffrin and Shapiro [49] derived many results for the case where both Re and ε/λ were negligible. In the case of no imposed pressure gradient (referred to as "free pumping" because there is no flow in the absence of wall motion), Φ can be given as a function of amplitude ratio $\phi = A/\varepsilon$

$$\Phi = 3\phi^2/(2+\phi^2). \tag{19}$$

We select $\varepsilon = 0.005$ cm, $c = 0.8$ cm/s, $\lambda = 0.4/\pi$ cm, and $\nu = 0.02\,\text{cm}^2/\text{s}$ thus $\varepsilon/\lambda = \pi/80$ and $\text{Re} = (\varepsilon c)(\varepsilon/\lambda)/\nu = \pi/400$ are small enough to be considered in the negligible inertia and infinite wavelength limit. The relaxation time is set to 0.95. A periodic boundary condition is imposed at the inlet and exit. The bounce-back boundary condition for rigid walls has been included in Eq. (10) for the streaming process. Using ϕ as the independent variable by changing A from 0.0005 to 0.005 cm, we obtain the MCVLBM simulation results which are nearly identical to the the analytical prediction as shown in Fig. 13. Figure 14(a) shows the pressure contours and the

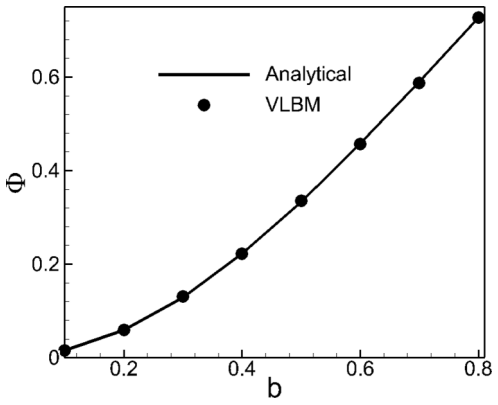

FIG. 13. Comparison of MCVLBM vs. analytical solution: Dimensionless time-mean volume flow rate as a function of amplitude ratio $\Phi = A/\varepsilon$. Re $= \pi/400$ and $\varepsilon/\lambda = \pi/80$.

streamlines over contours of velocity magnitude are shown in Fig. 14(b) for $\phi = 0.25$.

The geometry and nomenclature for a 3D pipe flow is portrayed in Fig. 15. The flow is driven by a constant pressure gradient $G = -dp/dx$ along the y direction. A periodic boundary is applied at the inlet and outlet and no-slip boundary on the walls. To compare to the analytical solution of Hagen-

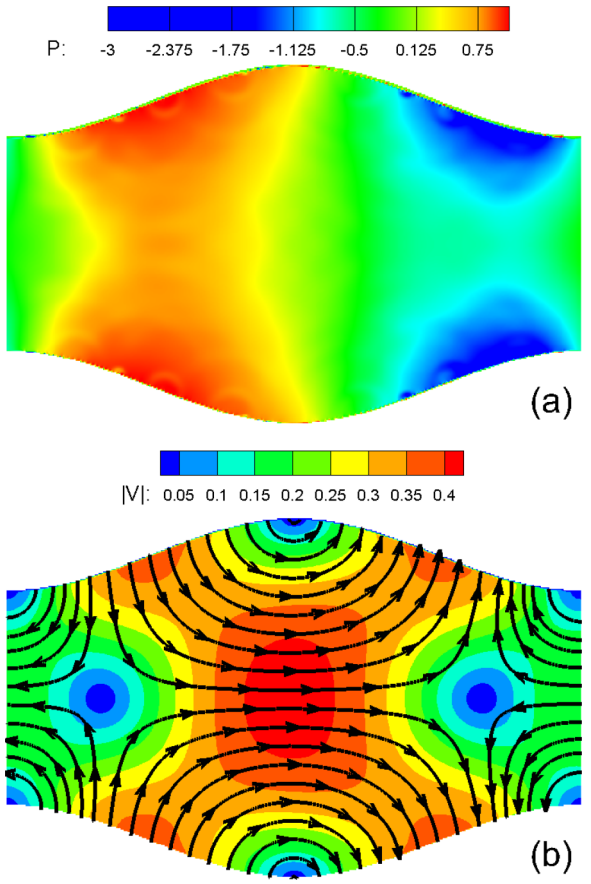

FIG. 14. (Color online) (a) Contour of pressure. The colors of the scale represent contours of gauge pressure normalized by $\mu c/\varepsilon$. (b) Streamlines of velocity field over contours of velocity magnitude.

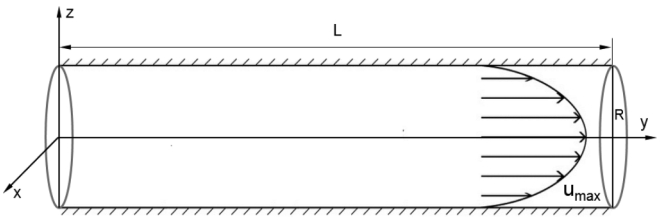

FIG. 15. Geometry and nomenclature for a 3D pipe flow. The parabolic velocity profile corresponds to the analytical solution of Hagen-Poiseuille flow [50]. $u_{\max} = G/(4\mu)$.

Poiseuille flow [50], we set $L = 0.01$ m, $R = 0.008$ m, $\mu = 3e-3$ kg/(ms), and $G = 1.2e-9$. The Reynolds number, defined as Re $= (2R)u_{\max}/\nu$, is about $5e-4$. When in the steady state, the parabolic velocity profile is expressed as $u(r) = G/(4\mu)(R^2 - r^2)$ where $r = \sqrt{x^2 + z^2}$. We compare the MCVLBM simulation result with the analytical solution in Fig. 16 and both velocity profiles are nearly identical.

C. Blood flow in a human normal aorta

For the validation of MCVLBM for arbitrary geometry, we simulate blood flow in a human aorta in two dimensions and three dimensions, respectively. The 2D geometry was digitized from a picture of a human aorta processed from a CT scan (Fig. 17). Here we do not consider the wall elasticity for the purpose to focus on the validation of VLBM for arbitrary geometry. The parameters used in the 2D case are listed in Table I. The blood is driven to enter the inlet upward at the bottom and exits through one major outlet at the bottom and two minor outlets at the top. Initially, the velocity field is set to $\vec{u} = 0$ everywhere in the computational domain except at the inlet where $\vec{u} = \vec{u}_b$. The initial pressure field is uniform at 1.0(atm). We apply for bounce-back including driving velocity $\vec{u}_b$ [51] at the inlet. In each inlet cell, n_1, n_5, and n_8 are unknown and can be defined from

$$n_i = n_{i*} - 6\omega_{i*} N_b \vec{u}_b \cdot \vec{e}_{i*}, \tag{20}$$

where $i*$ is the opposite direction of i. Thus n_1, n_5, and n_8 are determined by the bounce-back of n_2, n_7, and n_6 [see Fig. 1(b)] plus driving term. The fully developed condition is applied at the three outlets.

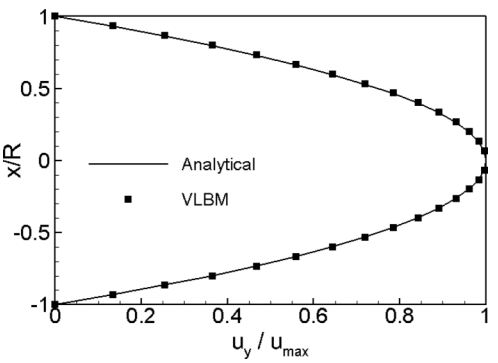

FIG. 16. Comparision of MCVLBM vs. the analytical solution: parabolic velocity profile of Hagen-Poiseuille flow [50].

FIG. 17. (Color online) A 3D aorta artery imaged from a human being.

Mass conservation is confirmed through the comparisons of mass fluxes at the inlet and the total amount of mass flux at three exits, similar to the results obtained in Fig. 7. It is found that around 88% of blood flows out at the major exit while the remaining 12% goes out through the minor exits. The velocity vector and streamline fields from MCVLBM simulation are shown in Fig. 18. The flow has well-organized velocity profiles for the defined velocity in Table I, implying that in a normal aorta with normal driven velocity, blood flow is laminar. Due to the geometry of the minor outlets at the top, there exist vortices at the corners where the blood starts to exit although the velocity magnitudes of them are small. To achieve quantitative validation, we run the same case using the prevailing commercial software ANSYS-FLUENT with steady and laminar options. The comparisons of velocity magnitude and pressure of MCVLBM versus ANYSYS-FLUENT are shown in Figs. 19 and 20, respectively. Quantitatively good agreements of the contours demonstrate that MCVLBM has well captured the fluid dynamics of the blood flow in the aorta.

The 3D case is part of our ongoing medical-related research project to study the alterations in shear stress and flow patterns to unveil the development of atherosclerotic plaque and embolic phenomena in human arteries including aortic, carotid, and renal arteries. We have developed a unified computing platform which integrates anatomical-structure

TABLE I. Aorta dimension and blood properties.

Height (m)	Length (m)	Blood viscosity (Pa · s)	Inlet velocity (m/s)	Inlet pressure (atm)
3.18*e*-2	2.5*e*-2	3.5*e*-3	1.0	1.0

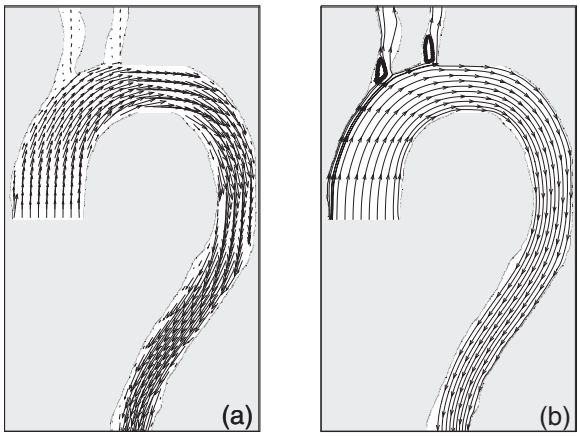

FIG. 18. (a) Velocity vector field. (b) Velocity streamlines.

extraction from radiological CT and MRI images and numerical simulation in one computation setup using the LBM [52]. The LBM successively solves a level set equation for image segmentation and NS equations for fluid dynamics, thus no mesh reconstruction is needed. The patient-specific vessel geometry, volumetric ratio of solid versus fluid, and the orientation of the boundary obtained in the process of segmentation seamlessly feed to the MCVLBM simulation. Considering the nature of blood flow, we use an ultrasound image of the same patient to extract a pulsatile velocity profile for the inlet boundary condition. At each time instant, the driven velocity is fed at the inlet with a parabolic shape with the maximum velocity equal to the corresponding velocity in the pulsation. We study the hemodynamic features with and without stenosis, aiming to discover hemodynamic indicators to predict the rupture risk of atherosclerotic plaques. Such hemodynamic indicators are currently absent in medical practice. The validation of the simulation is done through a comparison of velocity profiles from MCVLBM simulation and recorded wave by duplex ultrasound.

Here we study hemodynamics in a normal aortic artery segmented from a recorded CT dicom data of an anonymous patient during a clinical visit. The pulsatile velocity profile

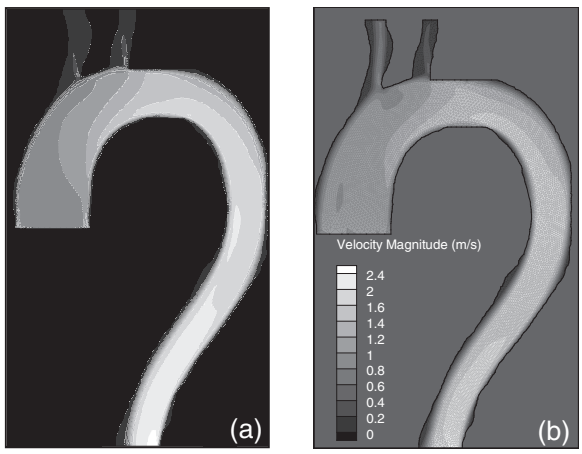

FIG. 19. Quantitative comparison of velocity magnitude contour. (a) MCVLBM. (b) ANSYS-FLUENT.

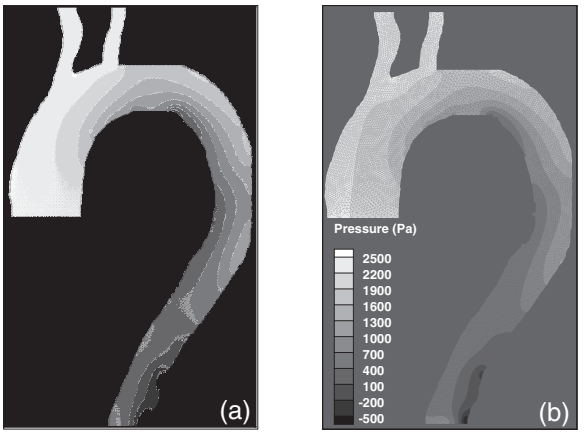

FIG. 20. Quantitative comparison of gauge pressure contour. (a) MCVLBM. (b) ANSYS-FLUENT.

$U_{in}(t)$ (Fig. 21) is generic and has been adapted to fit a direct numerical simulation. The density ρ, kinetic viscosity ν, and the boundary conditions are the same as in the 2D case. The height and inlet diameter of the aorta are $H = 0.087(m)$ and $D = 0.023(m)$, respectively. The Reynolds number is defined by $\mathrm{Re} = U_{in}D/\nu$. Figure 22 shows the velocity fields at six representative time instants corresponding to (a) $\mathrm{Re} = 419$, (b) $\mathrm{Re} = 607$, (c) $\mathrm{Re} = 419$, (d) $\mathrm{Re} = 0.34$, (e) $\mathrm{Re} = 229$, and (f) $\mathrm{Re} = 81$, respectively, during the cardiac pulsation. The velocity magnitude is calculated from $|V| = \sqrt{u_x^2 + u_y^2 + u_z^2}$. The contour level of the velocity magnitude in each field is appropriately scheduled, thus the flow pattern can be visualized. It is seen that the peak values of $|V|$ in different time instants are closely related to the inlet velocity value. The large velocity field corresponds to large inlet velocity and vice versa. In each field, velocity is larger in the descending aorta (left) than the ascending aorta (right). Meanwhile,

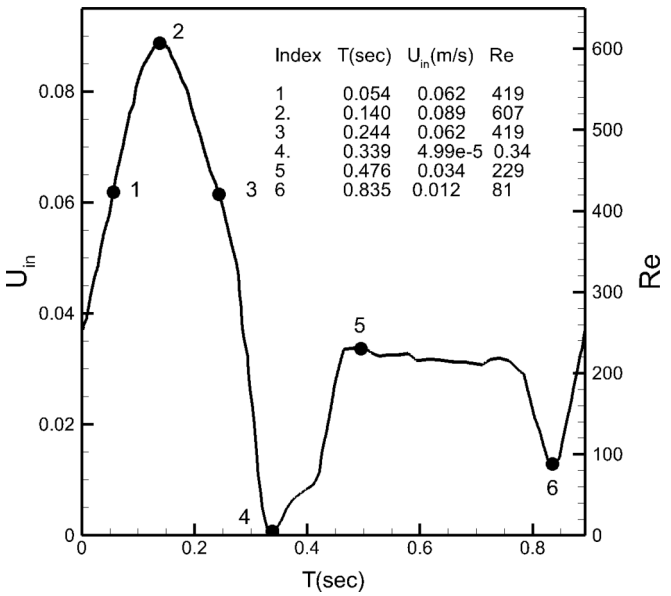

FIG. 21. Pulsatile velocity profile driving blood flow at the inlet. The Reynolds number is defined as $\mathrm{Re} = U_{in}D/\nu$.

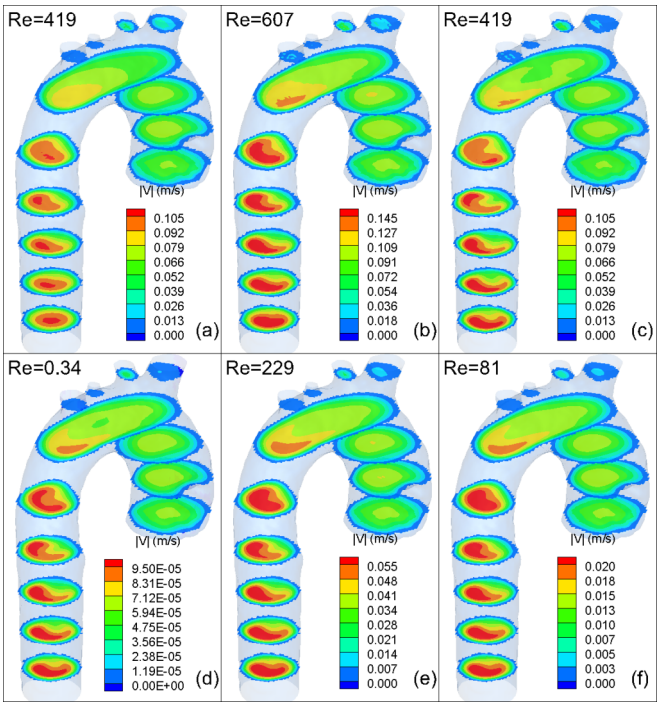

FIG. 22. (Color online) Contours of velocity magnitude on planes in vertical direction of six representative time points during pulsation marked in Fig. 21. (a) $\mathrm{Re} = 419$, (b) $\mathrm{Re} = 607$, (c) $\mathrm{Re} = 419$, (d) $\mathrm{Re} = 0.34$, (e) $\mathrm{Re} = 229$, and (f) $\mathrm{Re} = 81$.

velocity skewness, implying the deviation of the velocity profile from the parabolic shape, is clearly captured on the planes in the descending part due to the curvature of the branch at the top part. Fields (a) and (c) have the same Re numbers, but in the acceleration and deceleration stage, respectively. Although the Re numbers are the same, the skewness is seen as more profound in the deceleration than the acceleration.

Wall shear stress (WSS) acting on the inner layer of the artery is the force per unit area that is exerted by a moving viscous fluid on the artery. Here, we use Greek indexes to denote the spatial coordinates. The summation over any pair of identical Greek indexes is assumed. The local stress tensor for the fluid is

$$T_{\alpha\beta} = -p\delta_{\alpha\beta} + 2\mu S_{\alpha\beta}, \tag{21}$$

where $\delta_{\alpha\beta}$ is the Kronecker symbol and $S_{\alpha\beta}$ is the strain rate tensor. In LBM, the strain rate tensor can be calculated from the nonequilibrium particle density distribution functions [53]. The formulation of $S_{\alpha\beta}$ in MCVLBM is as follows:

$$S_{\alpha\beta} = -\frac{1}{2N\tau c_s^2}\sum_i^b \vec{e}_{i\alpha}\vec{e}_{i\beta}\left(n_i - n_i^{\mathrm{eq}}\right), \tag{22}$$

where $\alpha = 1,2,3$ and $\beta = 1,2,3$ correspond to nine components. The WSS vector, sometimes also called the traction vector, lies in the local tangent plane. It is computed by subtracting the normal component

$$\mathrm{WSS}_\alpha = T_{\alpha\beta}\chi_\beta - (\chi_\beta T_{\gamma\beta}\chi_\gamma)\chi_\alpha, \tag{23}$$

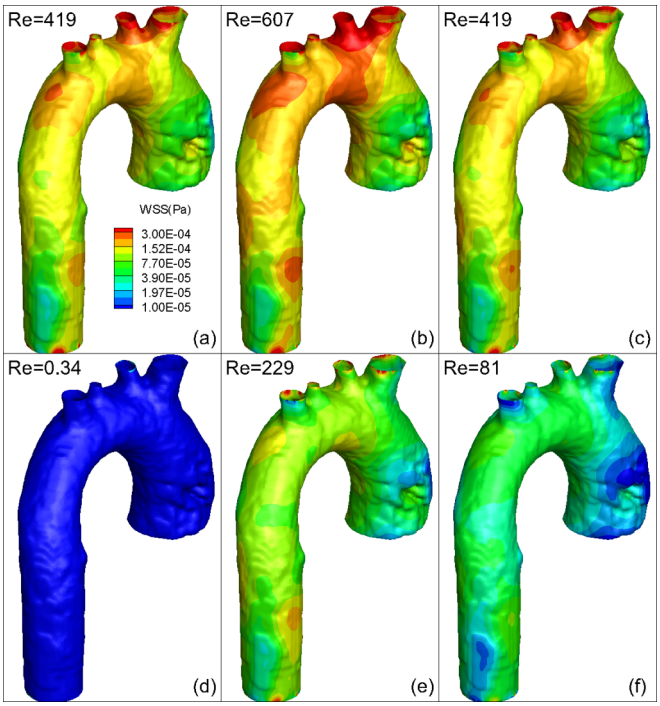

FIG. 23. (Color online) Distribution of wall shear stress on the artery of six representative time instants during the pulsation marked in Fig. 21. (a) Re = 419, (b) Re = 607, (c) Re = 419, (d) Re = 0.34, (e) Re = 229, and (f) Re = 81.

where the vector $\vec{\chi}$ indicates the normal direction of the local tangent plane.

The WSS magnitude on the inner artery at the representative time instants during the cardiac cycle are shown in Fig. 23. In general the WSS is much larger during systole Figs. 23(a) to 23(c)] than the diastole [Figs. 23(d) to 23(f)] of the heart beating. The WSS is intensive in the arch area over the ascending and descending parts. The maximum WSSs appears at the roots of the outflow branches during systole. The velocity skewness and WSS intensity we capture are in good agreement with an experimental study [54].

IV. SUMMARY AND FURTHER WORK

We have developed a mass-conserved lattice Boltzmann algorithm for willfully moving arbitrary boundaries based on a volumetric representation. In the MCVLBM, the simulation is on lattice cells characterized by the percentage of solid volume over the total cell volume thus categorizing the fluid cell, solid cell, and boundary cell in the whole domain. Momentum exchange at the boundary cells is incorporated into a collision operator to account for the force applied between the fluid and moving solid boundary, and volumetric bounce-back is applied in the streaming implementation based on the percentage of fluid and solid in neighboring cells. Boundary-induced migration is introduced to redistribute mass as the solid boundary crosses the fluid domain. This is a new and essential action to ensure mass conservation with arbitrarily moving solid boundaries. Unlike the node-based LBM boundary treatments, the MCVLBM satisfies mass conservation at all times. The scheme is independent of mesh orientation and position with respect to the solid surface. Four validation simulations characterizing a willfully moving boundary but regular geometry, complex geometry but fixed boundary in both two and three dimensions are performed. Nearly identical results to analytical solutions in 2D peristaltic flow and 3D pipe flow are achieved. The velocity and pressure fields at a steady state in a human aorta are compared to those from well-established commercial CFD software and the agreement is reasonably well. Due to the self-regularized LBM equations for collision, streaming, and boundary-induced migration through parameter $\mathcal{P}(\vec{x},t)$, the implementation of MCVLBM for the arbitrary version is rather simple.

More clinically related simulations for the blood flow in aortas are ongoing using the validated MCVLBM focusing on the examination of shear and normal wall stresses on the artery walls. We are particularly interested in the examination of the distribution of normal and shear wall stresses on the entire inner layer of healthy and diseased aortas and the role of turbulence on the wall stresses. Meanwhile, we are working on blood flow in the three-dimensional healthy and diseased aortas. The correlations between wall stress and the fluid dynamics of blood flow, the aorta geometry, and the driven condition at the inlet are expected to provide information valuable in the management of patients at risk or with already developed aortic aneurysms and/or dissections.

ACKNOWLEDGMENTS

H.Y. thanks Dr. Hudong Chen at Exa Corporation for providing instructive ideas and the formulation of the volumetric representation of the lattice Boltzmann method and Professor James G. Brasseur at Mechanical Engineering of the Pennsylvania State University for the support of originating this research idea. The research is supported by MURI and RSFG of IUPUI.

[1] F. J. Higuera, S. Succi, and R. Benzi, Europhys. Lett. **9**, 345 (1989).
[2] Y. H. Qian, D. D'Humieres, and P. Lallemand, Europhys. Lett. **17**, 479 (1992).
[3] H. Chen, S. Chen, and W. H. Matthaeus, Phys. Rev. A **45**, R5339 (1992).
[4] Y.-H. Qian, S. Succi, and S. A. Orszag, Annu. Rev. Comput. Phys. **3**, 195 (1995).
[5] S. Chen and G. D. Doolen, Ann. Rev. Fluid Mech. **30**, 329 (1998).
[6] C. K. Aidun and J. R. Clausen, Ann. Rev. Fluid Mech. **42**, 439 (2010).
[7] G. P. Giovanni and R. Rannacher, *Fundamental Trends in Fluid-Structure Interaction* (World Scientific, Singapore, 2010).
[8] P. M. Moretti, Ann. Rev. Fluid Mech. **25**, 99 (1993).

[9] A. Khamlichi, B. Ayyat, M. Bezzazi, L. El Bakkali, C. V. Venegas, and F. C. Castaño, Australian J. Basic Appl. Sci. **3**, 3246 (2009).
[10] E. de Langre, Ann. Rev. Fluid Mech. **40**, 141 (2008).
[11] J. C. Lasheras, Ann. Rev. Fluid Mech. **39**, 293 (2007).
[12] M. Heil and A. L. Hazel, Ann. Rev. Fluid Mech. **43**, 141 (2011).
[13] J. B. Grotberg and O. E. Jensen, Ann. Rev. Fluid Mech. **36**, 121 (2004).
[14] L. J. Fauci and R. Dillon, Ann. Rev. Fluid Mech. **38**, 371 (2006).
[15] X. He and L.-S. Luo, Phys. Rev. E **56**, 6811 (1997).
[16] X. Shan and X. He, Phys. Rev. Lett. **80**, 65 (1998).
[17] X. Shan, X.-F. Yuan, and H. Chen, J. Fluid Mech. **550**, 413 (2006).
[18] H. Chen, C. Teixeira, and K. Molvig, Int. J. Mod. Phys. C **09**, 1281 (1998).
[19] H. Chen, Phys. Rev. E **58**, 3955 (1998).
[20] D. R. Noble, S. Chen, J. Georgiadis, and R. Q. Buckius, Phys. Fluids **7**, 203 (1995).
[21] T. Inamuro, M. Yoshino, and F. Ogino, Phys. Fluids **7**, 2928 (1995).
[22] R. S. Maier, R. S. Bernard, and D. W. Grunau, Phys. Fluids **8**, 1788 (1996).
[23] S. Chen, D. Martinez, and R. Mei, Phys. Fluids **8**, 2527 (1996).
[24] Q. Zou and X. He, Phys. Fluids **9**, 1591 (1997).
[25] X. He and G. D. Doolen, Phys. Rev. E **56**, 434 (1997).
[26] O. Filippova and D. Hinel, Int. J. Mod. Phys. C **09**, 1271 (1998).
[27] R. Mei, L.-S. Luo, and W. Shyy, J. Comput. Phys. **155**, 307 (1999).
[28] I. C. Kim, KSME Int. J. **14**, 84 (2000).
[29] Z. L. Guo, C. G. Zheng, and B. C. Shi, Phys. Fluids **14**, 2007 (2002).
[30] S. Izquierdo and N. Fueyo, J. Comput. Phys. **229**, 2497 (2010).
[31] T. Zhang, B. Shi, Z. Guo, Z. Chai, and J. Lu, Phys. Rev. E **85**, 016701 (2012).
[32] A. J. C. Ladd, J. Fluid Mech. **271**, 311 (1994).
[33] M. Bouzidi, M. Firdaouss, and P. Lallemand, Phys. Fluids **13**, 3452 (2001).
[34] X. Yin and J. Zhang, J. Comput. Phys. **231**, 4295 (2012).
[35] C. K. Aidun and Y. Lu, J. Stats. Phys. **81**, 49 (1995).
[36] S. Ansumali and I. V. Karlin, Phys. Rev. E **66**, 026311 (2002).
[37] S. Krithivasan, S. Wahal, and S. Ansumali, Phys. Rev. E **89**, 033313 (2014).
[38] R. Verberg and A. J. C. Ladd, Phys. Rev. Lett. **84**, 2148 (2000).
[39] R. Verberg and A. J. C. Ladd, Phys. Rev. E **65**, 016701 (2001).
[40] H. Chen, C. Teixeira, and K. Molvig, Int. J. Mod. Phys. C **08**, 675 (1997).
[41] R. Zhang, H. Chen, Y. H. Qian, and S. Chen, Phys. Rev. E **63**, 056705 (2001).
[42] Y. Qian, Int. J. Mod. Phys. C **8**, 753 (1997).
[43] Y. Li, R. Shock, R. Zhang, and H. Chen, J. Fluid Mech. **519**, 273 (2004).
[44] Y. Li, R. Zhang, and H. Chen, Eur. Phys. J. Special Topics **171**, 91 (2009).
[45] N. Schmidt, C. Saez *et al.*, Pediatr. Crit. Care Med. **11**, 282 (2010).
[46] H. K. Moffatt, J. Fluid Mech. **18**, 1 (1964).
[47] L. T. Watson, S. C. Billups, C. Y. Wang, and E. A. Everett, J. Biomech. Eng. **108**, 317 (1986).
[48] A. H. Shapiro, M. Y. Jaffrin, and S. L. Weinberg, J. Fluid Mech. **37**, 799 (1969).
[49] M. Y. Jaffrin and A. H. Shapiro, Annu. Rev. Fluid Mech. **3**, 13 (1971).
[50] F. M. White, *Viscous Fluid Flow, Third Edition* (McGraw-Hill, New York, 2006).
[51] L.-S. Luo, Phys. Rev. E **62**, 4982 (2000).
[52] H. Yu, Z. Wang, C. Zhang, N. Chen, A. P. Sawchuk, Y. Zhao, and Y. Chen (unpublished).
[53] H. Yu, S. S. Girimaji, and L.-S. Luo, J. Comput. Phys. **209**, 599 (2005).
[54] P. E. Vincent, A. M. Plata, A. A. E. Hunt, P. D. Weinberg, and S. J. Sherwin, J. R. Soc. Interface **8**, 1708 (2011).